



ELSEVIER

Available online at www.sciencedirect.com

SCIENCE @ DIRECT®

Journal of Applied Geophysics 57 (2005) 260–277

JOURNAL OF
APPLIED
GEOPHYSICS

www.elsevier.com/locate/jappgeo

Image processing of 2D resistivity data for imaging faults

F. Nguyen^{a,*}, S. Garambois^b, D. Jongmans^b, E. Pirard^a, M.H. Loke^c

^a*Geomac, Liege University, Belgium*

^b*LIRIGM, Joseph Fourier University, Grenoble, France*

^c*School of Physics, University of Science of Malaysia, Malaysia*

Received 3 November 2003; accepted 15 February 2005

Abstract

A methodology to locate automatically limits or boundaries between different geological bodies in 2D electrical tomography is proposed, using a crest line extraction process in gradient images. This method is applied on several synthetic models and on field data set acquired on three experimental sites during the European project PALEOSIS where trenches were dug. The results presented in this work are valid for electrical tomographies data collected with a Wenner-alpha array and computed with an l_1 norm (blocky inversion) as optimization method. For the synthetic cases, three geometric contexts are modelled: a vertical and a dipping fault juxtaposing two different geological formations and a step-like structure. A superficial layer can cover each geological structure. In these three situations, the method locates the synthetic faults and layer boundaries, and determines fault displacement but with several limitations. The estimated fault positions correlate exactly with the synthetic ones if a conductive (or no superficial) layer overlies the studied structure. When a resistive layer with a thickness of 6 m covers the model, faults are positioned with a maximum error of 1 m. Moreover, when a resistive and/or a thick top layer is present, the resolution significantly decreases for the fault displacement estimation (error up to 150%). The tests with the synthetic models for surveys using the Wenner-alpha array indicate that the proposed methodology is best suited to vertical and horizontal contacts. Application of the methodology to real data sets shows that a lateral resistivity contrast of 1:5–1:10 leads to exact faults location. A fault contact with a resistivity contrast of 1:0.75 and overlaid by a resistive layer with a thickness of 1 m gives an error location ranging from 1 to 3 m. Moreover, no result is obtained for a contact with very low contrasts (\sim 1:0.85) overlaid by a resistive soil. The method shows poor results when vertical gradients are greater than horizontal ones. This kind of image processing technique should be systematically used for improving the objectiveness of tomography interpretation when looking for limits between geological objects.

© 2005 Elsevier B.V. All rights reserved.

Keywords: Active faults; Fault survey; Image processing; Electrical tomography; Near-surface geophysics

* Corresponding author. Postal address: Chemin des chevreuils, 1 Bât. B-52 4000 Liège Belgium. Tel.: +32 4 366 2032; fax: +32 4 366 9520.
E-mail addresses: fnguyen@ulg.ac.be (F. Nguyen), stephane.garambois@ujf-grenoble.fr (S. Garambois), Denis.Jongmans@ujf-grenoble.fr (D. Jongmans), mhloke@tm.net.my (M.H. Loke).

1. Introduction

Among all geophysical techniques dedicated to image the near surface, 2D or 3D resistivity surveying has been increasingly used for environmental, engineering and geological purposes this last decade (e.g., Meads et al., 2003; van Schoor, 2002; Dahlin et al., 2002; Demanet et al., 2001b). To adequately image the subsurface, the pseudo-section resistivity data set must be inverted using a cell-based inversion technique (see, for example, Loke and Barker, 1996). The principle consists in subdividing the studied 2D surface into a number of cells and in determining the resistivity within the cells that would provide a model response fitting well the measured data. Even if the inversion is a quasi-automatic process, there remains uncertainty in the reliability of the final obtained image.

First, options within the inversion process can highly influence the final sections, as the choice of the optimization norm and the way of computing the partial derivatives. Two optimization methods are commonly used to solve the inversion process: the l_2 norm (smoothness-constraint) which is well adapted for areas where the resistivity varies in a gradual manner (deGroot-Hedlin and Constable, 1990), and the l_1 norm (blocky optimization), which gives significantly better results when sharp boundaries are present (Claerbout and Muir, 1973, Loke et al., 2003; Olayinka and Yaramanci, 2000). In the same way, to solve the least-square equation, the Jacobian matrix of partial derivatives must be computed for all iterations. For this purpose, the Gauss–Newton method gives significantly more accurate results than the quasi-Newton method when the survey area exhibits large resistivity contrasts, and almost similar results for moderate contrasts (Loke and Dalhin, 2002).

Second, the inversion of electrical data is a non-linear problem which is usually solved by linearized methods (Tarantola, 1987; Loke and Barker, 1996). These techniques require a starting model, which can highly influence the solution if the misfit function exhibits several minima. A way of addressing this problem is to use direct search algorithms like the simulated annealing technique (Pessel, 2000) or the neighborhood algorithm (Sambridge, 1999a,b). However, due to the long computation time required, these

techniques are limited so far to a small number of parameters, and have been rarely applied to electrical imaging (Pessel, 2000).

Third, delineating the exact position of boundaries in an electrical tomography is often a difficult task, depending on the colour scale and on the eye sensitivity of the interpreter. Indeed, when the final image presents smooth resistivity variations, boundaries appear as continuous transitions between zones of different resistivities. For example, the response of a vertical contact model with a conductive superficial layer (Fig. 1) has been computed and inverted using the RES2DINV software (Loke and Barker, 1996). The smoothed electrical tomography is shown in Fig. 1B and C with a logarithmic and a linear colour scale, respectively. Depending on the interpreter, the geometry can be very different from the two images. Moreover, these images also depend on the interpolation technique used for the smoothing.

Image and signal processing techniques are commonly used in wave methods to help the user to have an objective interpretation. For example, Morozov and Smithson (1996) used image processing techniques (histogram equalization technique) on seismic signals to compare and plot coherency measures. A 3D skeletonization technique was developed by Vasudevan et al. (1997) to allow automatic event detection and mapping of surfaces in 3D volume of reflection seismic data. Another example can be found in Bergeron and Yuen (2000) who used wavelet transforms to detect plume-like structures from 3D seismic tomography. Other object or event detection algorithms were developed in Al-Nuaimy et al. (2000) and Carter and Lines (2001). Demanet et al. (2001a) used image processing algorithms to automatically detect faults in electrical and seismic tomography images. Based on two synthetic models and one experimental study, they present preliminary results showing that a crest line location method applied on morphological gradient images (Beucher and Meyer, 1992) is successful in identifying sharp lateral contrasts (for example, generated by faults). However, the authors do not make a clear comparison between the identified faults resulting from the image processing, and the known synthetic limits.

The aim of this paper is to investigate the pertinence and limits of image processing algorithms to extract boundaries from electrical tomography. The

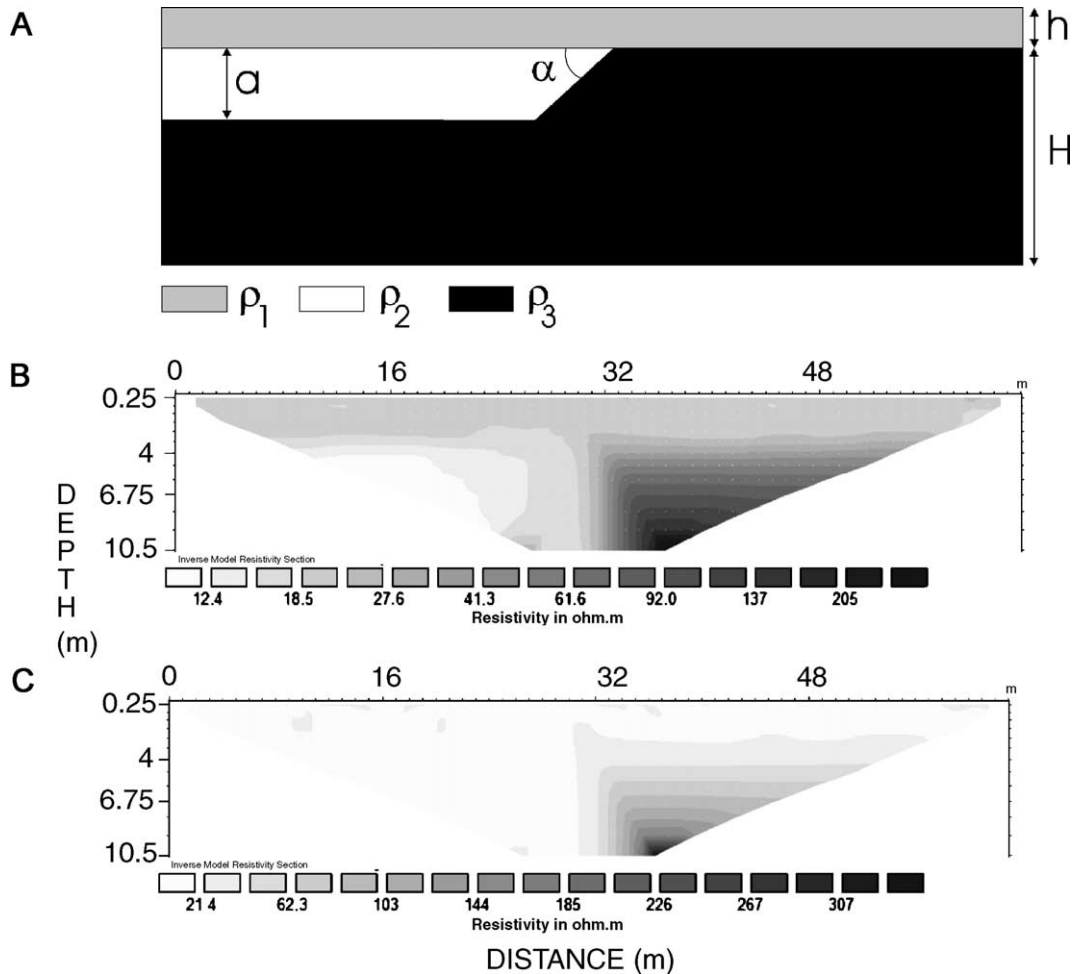


Fig. 1. (A) Generic model used for the forward modelling: ρ_1 is the resistivity of the top layer, ρ_2 and ρ_3 , the resistivities of the faulted blocks. The thickness of the top layer is h , the thickness of the faulted layers is H and a is the vertical displacement along the fault. (B) Smoothed electrical tomography of the vertical fault contact with a 4 m–20 Ω m top layer with a logarithmic colour scale. (C) Smoothed electrical tomography of the vertical fault contact with a 4 m–20 Ω m top layer with a linear colour scale.

study is focused on fault detection from electrical tomography images, which are increasingly used in paleoseismology for positioning faults and for studying tectonic deformations in shallow layers (Suzuki et al., 2000; Demanet et al., 2001b; Louis et al., 2002; Wise et al., 2003; Nguyen et al., 2003). These interpretation methods are applied on several synthetic models and on an experimental data set acquired during the European project PALEOSIS (Camelbeek, 2000). For the numerical simulations, three geometries are considered (Fig. 1): a vertical ($\alpha=90^\circ$) and a dipping ($\alpha=45^\circ$) fault juxtaposing two different

geological formations ($a>H$) and a vertical fault ($\alpha=90^\circ$) shifting horizontal layers ($a<H$).

2. Methodology

The gradient images are computed from the (non-smoothed) electrical tomography (Fig. 2) with a maximum of directional gradient (MDG) algorithm that replaces the resistivity value of the central cell (ρ_{ij}), in a 3×3 neighbourhood, by the maximum gradient intensity G_{ij} and its corresponding direction

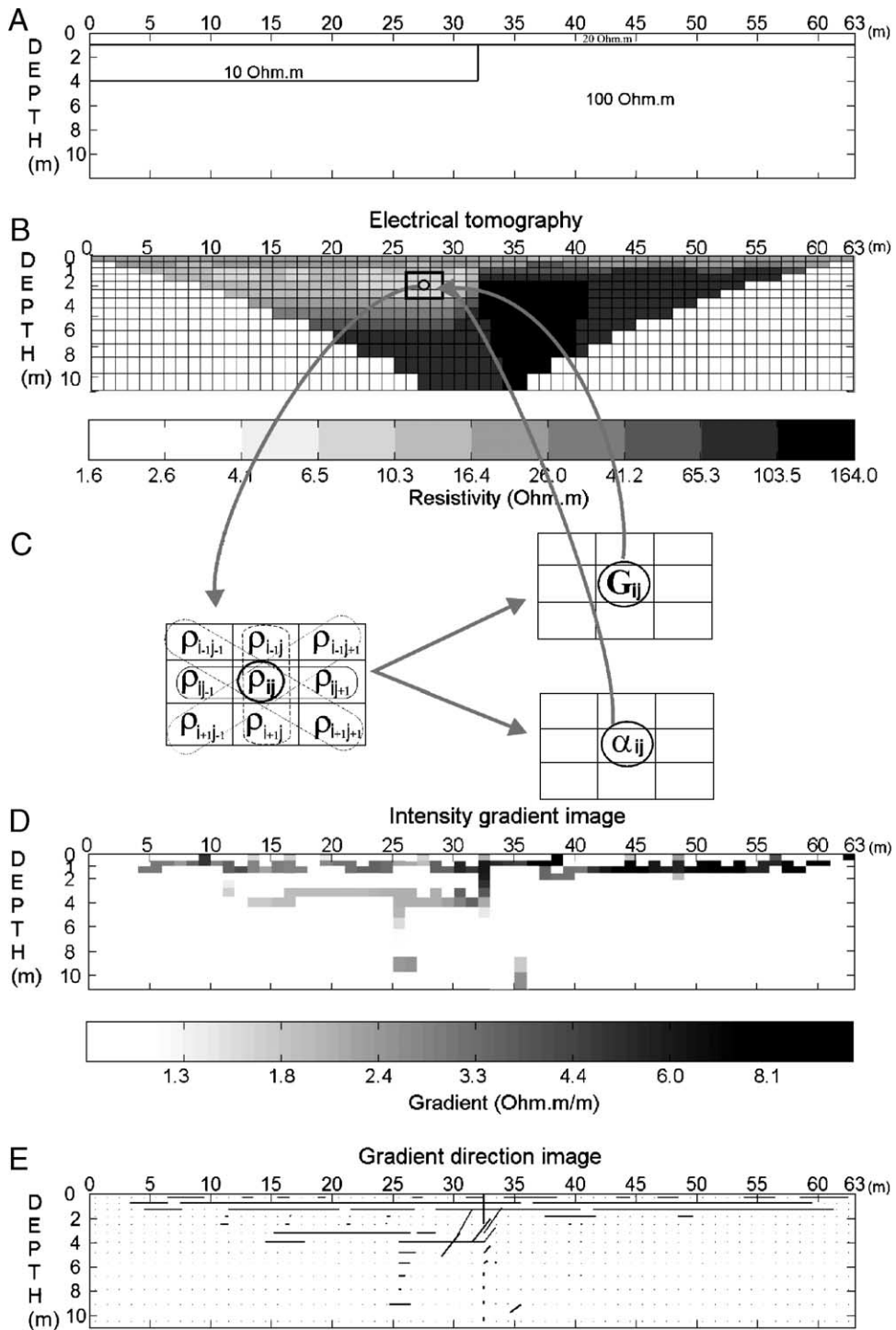


Fig. 2. Synthetic model (A), electrical tomography (B) of a step-like model with a 20 Ω m superficial layer of 1 m with a step height of 3 m. (C) Scheme of the maximum of directional gradient (MDG) computation on a 3x3 neighbourhood. The algorithm replaces the resistivity of the ij cell (ρ_{ij}) by the gradient intensity (G_{ij}) and direction (α_{ij}). (D and E) Respectively, intensity and direction gradient images.

α_{ij} (Fig. 2C). The gradient intensity is computed as follows,

$$G_{ij} = \max \left\{ \frac{|\rho_{i-1,j-1} - \rho_{i+1,j+1}|}{D[(i-1,j-1),(i+1,j+1)]}, \frac{|\rho_{i-1,j} - \rho_{i+1,j}|}{D[(i-1,j),(i+1,j)]}, \frac{|\rho_{i+1,j-1} - \rho_{i-1,j+1}|}{D[(i+1,j-1),(i-1,j+1)]}, \frac{|\rho_{i,j-1} - \rho_{i,j+1}|}{D[(i,j-1),(i,j+1)]} \right\} \quad (1)$$

where ρ is the resistivity value in Ohm meter, ij the indices of the central cell and $D[]$ the distance between two cells. The intensity gradient images are then regarded as topographical relief maps with crest lines separating zones of constant resistivity. A watershed algorithm, based on an immersion process analogy (Vincent and Soille, 1991) is applied on the gradient image to extract crest lines. Each pixel of these lines is being allotted with its corresponding gradient value and its direction, leading to two different images. The first one gives the intensity value of the gradient on the crest lines (further referred as gradient intensity image) while, in the second one, segments whose length is proportional to the gradient intensity are drawn with a direction perpendicular to the gradient. The method is illustrated on a synthetic case (Fig. 2) with a step-like geometry overlaid with a 20 Ω m top layer (Fig. 2A). The electrical tomography and the two gradient images are shown on Fig. 2B, D and E, respectively. For both gradient images, the method correctly delineates the main horizontal and vertical boundaries, while a visual interpretation would have probably missed the horizontal contact between the 20 Ω m top layer and the 10 Ω m layer.

3. Synthetic models

A layout of 64 electrodes is modeled using a Wenner-alpha array and an electrode spacing of 1 m. The synthetic data are computed using the forward modeling program Res2Dmod (Loke and Barker, 1996). A 3% Gaussian noise (Press et al., 1988) is added to the data. The pseudo-section data are inverted using an l_1 norm (blocky inversion) as optimization method, which is likely to produce sharper gradients.

The generic model used in this work is shown in Fig. 1A. For the vertical and dipping contact models ($\alpha=90^\circ$ and 45°), several thicknesses ($h=0, 1, 2, 4$ and 6 m) and two resistivities ($\rho_1=20$ and 250 Ω m) are used to simulate different soil configurations. Concerning the step-like structure, three soil resistivities are tested (10, 20 and 200 Ω m) as well as two values of the vertical fault displacement ($a=1.5$ and 3 m) and four thicknesses h (0.5, 1, 2 and 4 m). Fig. 3A shows an electrical tomography computed on a synthetic vertical contrast (10:100 Ω m, located at a distance of 20 m) with no superficial layer. Fig. 3B, C and D show normalized gradient cross-sections computed at several depths for three resistivity contrasts (respectively 10:20, 10:100 and 10:1000 Ω m). For each contrast, the gradient curves indicate that the contact location error (maximum of the curve) increases with depth, as the resolution of the electrical method decreases. Fig. 3 also shows that higher resistivity contrasts (greater than 10:20) lead to higher location errors. The apex of the gradient curve shifts towards the higher resistivity block at depth. As the electrical current tends to circulate in conductive material, the resistivity variation is expected to be smooth from low resistivities to higher ones and to become more rapid when the resistive material is reached.

3.1. Results

The possibilities of image processing have been tested for a horizontal contrast of 10 (10 to 100 Ω m across the fault), which is consistent with the values observed in PALEOSIS field data. First, the results for structures without superficial layer are presented (Fig. 4). For the vertical fault model, the main MDG crest line (Fig. 4A) corresponds precisely with the fault location. Several minor limits appear near the surface and at depth. They can be discarded as they are discontinuous and exhibit weaker gradient values. If the fault plane dips at 45° (Fig. 4B), the limit delineated by the MDG corresponds with the synthetic one down to 2 m. At that depth, the MDG crest line splits into a vertical and a dipping one, estimating the synthetic fault dip with an error of respectively 45° and 17° . The gradient direction image (Fig. 4B) shows near the surface a short dipping segment correlating with the fault, while the major contact appears to be

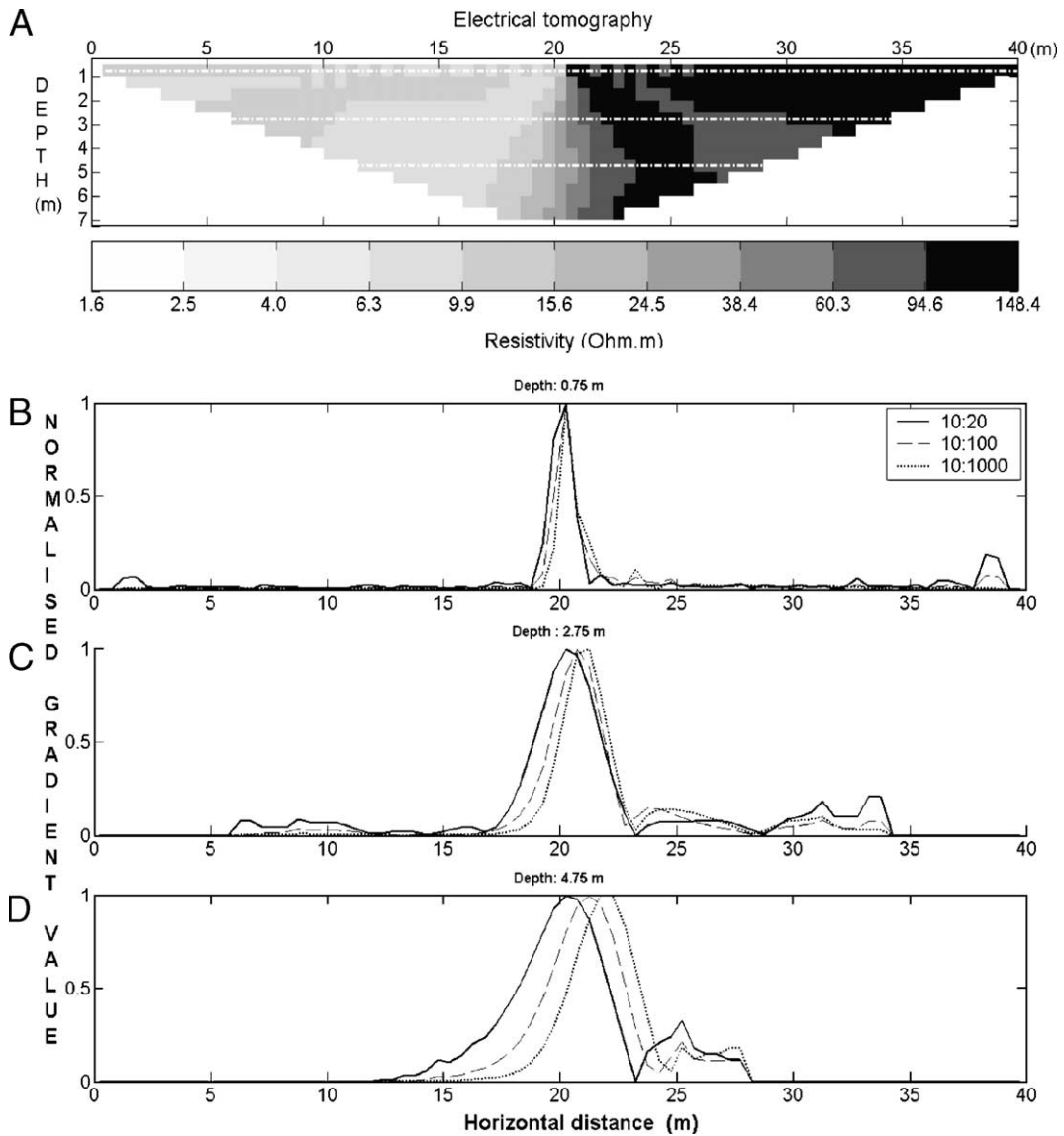
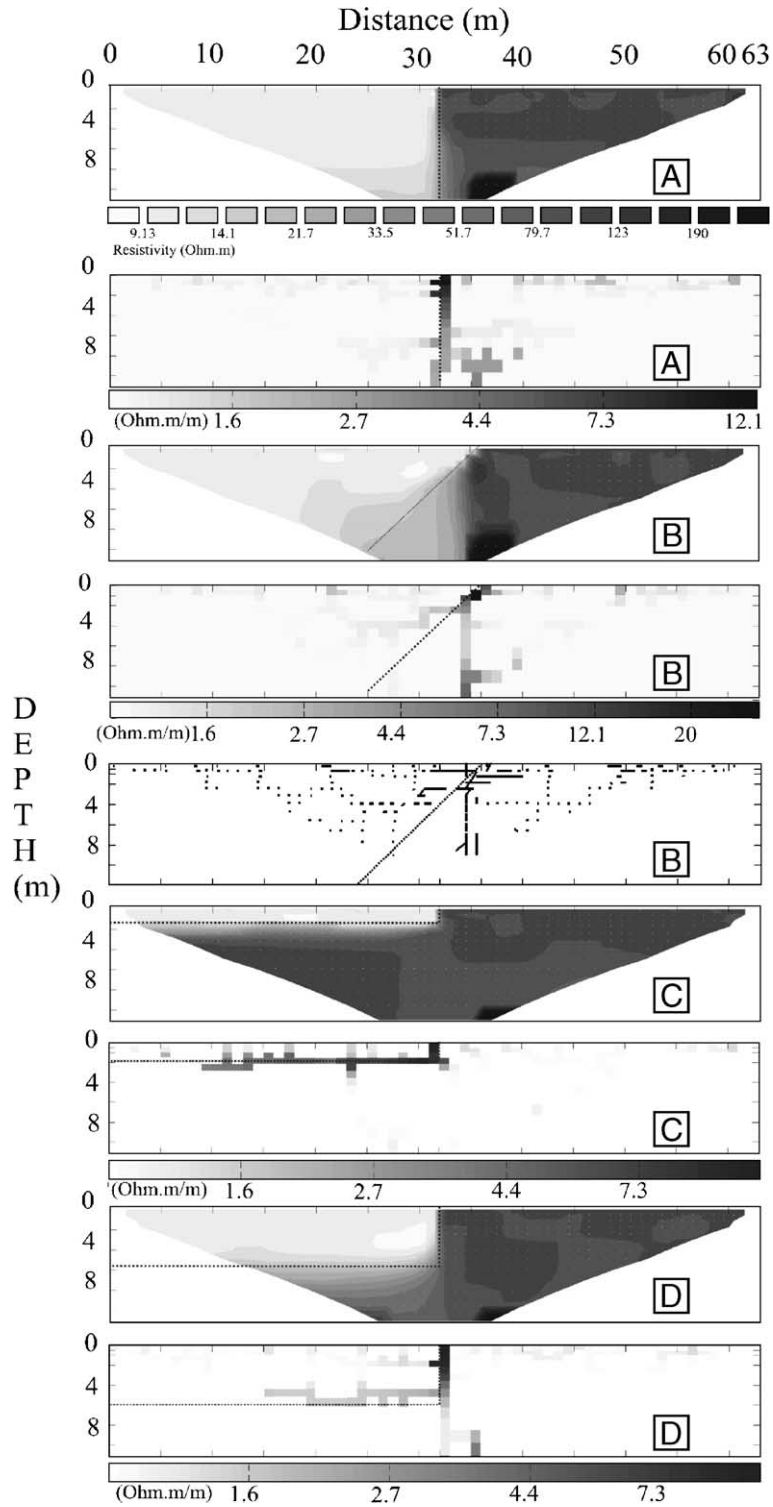


Fig. 3. (A) Electrical tomography of vertical contact with a 10:100 Ω m contrast with no top layer. White lines indicate the depth at which gradients are computed. (B, C and D) Normalized gradient cross-sections computed at various depths (respectively 0.75, 2.75 and 4.75 m) for three different contrasts: 10 Ω m to 20 Ω m (plain line), 10 Ω m to 100 Ω m (dash line) and 10 Ω m to 1000 Ω m (dot line).

vertical at depth. Fig. 4C and D show the extraction of the MDG crest lines for two step-like structures with a height of 2 m and 6 m. Both the top of the down thrown block and the vertical fault are well resolved by the MDG method for a vertical displacement of 2 m (Fig. 4C). For higher values (6 m, Fig. 4D), the error in the depth of the down thrown block increases to about 1 m.

In real geological conditions, a superficial soil layer generally covers the investigated geological structure. First, a conductive layer (20 Ω m) is added on top of the vertical contact structure (Fig. 5). For a 1-m (Fig. 5A) and a 4-m (Fig. 5B)-thick top layer, MDG images show both the horizontal contact between the soil and the bedrock, and the fault position at the correct locations. This latest figure



corresponds to the case presented in Fig. 2 and illustrates well the quantification and objectiveness brought by the MDG method, comparing to the visual interpretation. For thicker superficial layers (6 m, Fig. 5C), the fault is localized with a maximum error of 1 m. However, the errors for depth of the horizontal contacts range from 1 to 3 m for the 20:10 Ω m contrast (left block) and are of 1 m for the 20:100 Ω m contrast (right block). For a dipping fault (Fig. 5D), the bottom of the top soil (up to 4 m thick) is accurately extracted as well as the horizontal position of the fault. At greater depth, the main MDG crest line is vertical and does not correspond with the synthetic fault. Some directions of the MDG (Fig. 5D, bottom) near the horizontal contact are dipping and indicate roughly the true orientation. For a step-like model displaying a vertical displacement of 1.5 m and covered by 2-m-thick top layer with a resistivity of 10 Ω m (Fig. 5E), the vertical offset is underestimated at 0.75 m. For a 20 Ω m superficial layer (Fig. 5F), the crest extraction processing leads to an overestimation (2.5 to 3.5 m) of the throw. For a model with a thinner superficial layer (1 m) of 10 Ω m (Fig. 5G) and 20 Ω m (Fig. 5H) and the same vertical throw, all limits are accurately retrieved with the MDG method for both soils. For larger displacements (3 m, Fig. 5I), all limits are correctly identified.

A resistive superficial layer of 250 Ω m is now added on top of the different geological structures. For a 2-m-thick soil covering a vertical fault (Fig. 6A), the contact location is correctly given by the vertical MDG crest line near the horizontal limit. But at greater depth, the MDG crest line is located a meter to the right of the synthetic fault towards the higher resistivities. For the dipping fault model (Fig. 6B and C), two MDG crest lines are located near the fault, one being vertical as previously observed for the conductive superficial layer and the other dipping. The latter corresponds well with the dipping fault for a 2-m soil thickness (Fig. 6B). However, for thinner layers (Fig. 6C), the MDG crest line does not correlate with the synthetic fault. On the step-like fault model with a 1-m-thick soil (Fig. 6D), the MDG crest line

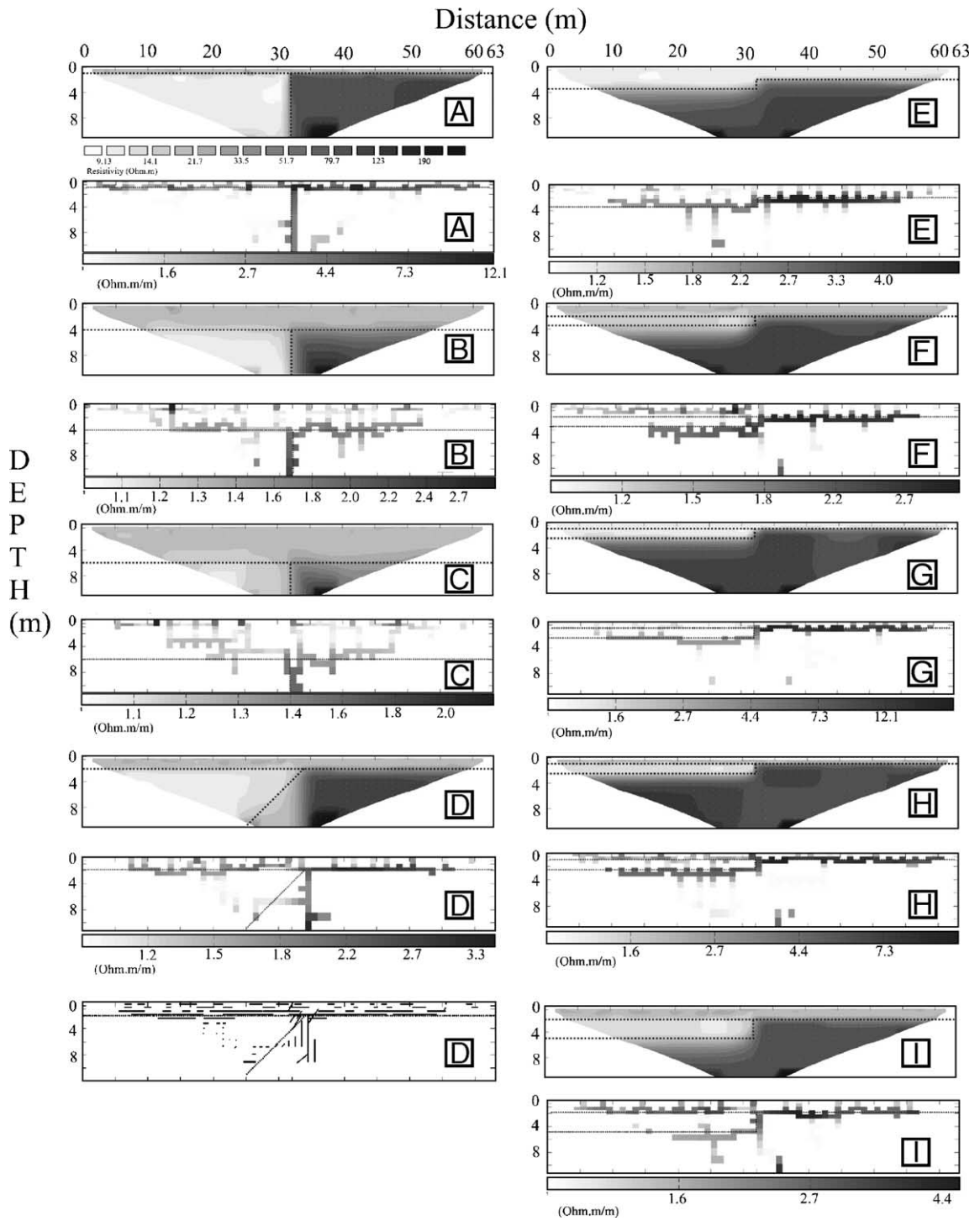
identifying the top of the hanging wall is located 1 m deeper than the synthetic limit for a 1.5 m vertical offset. For larger displacements (3 m, Fig. 6E), all limits are correctly identified. If the soil is thicker (2 m, Fig. 6F), the top of the down thrown block is positioned with a 1–2 m error.

3.2. Synthesis and discussion of numerical results

It has been shown that the MDG crest line extraction method can be used to estimate the location of lithological contacts or fault, as well as to determine the displacement induced by the fault, bringing a more objective and quantitative interpretation than the visual one. The method should be preferably used when horizontal and vertical contacts are awaited, when using a Wenner-alpha array. However, this technique presents several limitations.

First, the geometry of dipping contacts is correctly identified only in the upper few meters for a model without superficial layer (Fig. 4B). One factor explaining this limit is the exponential resolution decrease of the surface resistivity investigation method as a function of depth (Barker, 1989; Loke and Dalhin, 2002). This direct consequence from the basic laws of physics cannot be improved, unless borehole measurements are available. A second factor is the non-uniqueness of the solution resulting from the inversion process. As the data density decreases with depth, the constraint on the model is greatly reduced in this zone therefore allowing more alternate solutions. The cells shape could also influence the resistivity distribution. Rectangular cells, as used in this work, probably favour vertical and horizontal gradients as observed in the numerical study, whereas triangular cells could bring more flexibility in the gradient direction distribution. Reducing the cell sizes could also enhance the image resolution and therefore the resolution of the studied object. However, tests (not shown in this work) show that results obtained by choosing cell sizes equal to a half unit electrode spacing are similar to standard cell size ones (unit electrode spacing) and require longer computation

Fig. 4. Intensity and direction gradient images for models with no top layer. The dotted lines represent the synthetic model. The electrical tomography of the model is shown above each gradient image. The resistivity scale is the same for all tomographies. (A) Gradient intensity image (bottom) for a vertical contact. (B) Dipping contact intensity (middle) and direction (bottom) gradient images. (C and D) Gradient intensity image (bottom) of a step-like structure with respectively a 2-m and a 6-m step height.



time. Moreover, the cell size down-scaling factor is limited by the resolution of the resistivity method (Sasaki, 1992). If a supplemental surface soil layer is added to the model, the MDG method fails to determine the fault geometry at depth (Figs. 5 and 6). In this case, the position of the fault is accurately located at its uppermost part, and the directions of the gradient can be used to roughly determine whether the contact is dipping. When a top layer is added and/or when the structure gets deeper, the constraint on the investigated contact is reduced as well as the resolution.

Second, the modelling shows that the MDG crest lines extraction process depends on the resistivity of the superficial layer and on its thickness. In this work, the top soil affects in a non-proportional way the two blocks when modelling the two types of soils. Indeed, the vertical contrast for the left block is of 2:1 and 1:5 for the right block if a conductive soil is modelled, and of 25:1 and 1:2.5 if a resistive soil is present (Fig. 6). This influences the depth of investigation of the array (Barker, 1989; Oldenburg and Li, 1999), above the two faulted blocks. Best results are reached when the superficial layer is a low-resistive soil probably resulting from the lower contrast between the top soil and the underlying formation. Another parameter (not tested in this work) which could also influence the methodology outcome is the value of the resistivity contrast between the two faulted blocks (see Fig. 3).

Third, unlike signal or image processing techniques applied directly on measured data when dealing with waves methods, which can be related to strong physical and theoretical backgrounds (i.e., seismic or electromagnetic signal), the methodology introduced here is applied on inverted data. As mentioned in the introduction, the result of this inversion highly depends on several parameters and the analysis provided in this work is only valid for a blocky inversion. Furthermore, the type of array (such as the Wenner and dipole–dipole) will also influence the final image, as each array presents different sensitiv-

ities, depth of investigation and resolution power. Only the Wenner-alpha is used in this work. Although, it exhibits a moderate depth of investigation and lateral resolution, it possesses the highest signal to noise ratio. As different electrode arrays offer other advantages in different situations, the application of the image processing with the different array deserves further studies. For example, the dipole–dipole array, which is more sensitive to noise, has a greater lateral sensitivity than the Wenner-alpha and should improve the resolution of electrical tomographies and therefore the use of the MDG, particularly for dipping contacts.

4. Application to real data

The crest line extraction method is used below on different real data sets acquired on 3 test sites for the PALEOSIS experiment dedicated to the identification of active faults from geophysical measurements (Camelbeek, 2000). The sites are located in the Lower Rhine Embayment (LRE), an active rift system (Camelbeek and Meghraoui, 1996, 1998) straddling the border region of Belgium, Germany and The Netherlands (Fig. 7). The strong subsidence of this region during the last 150,000 years (Geluk et al., 1994), the Quaternary faults and associated morphology along the flanks of the graben, and the 0.8 mm/year to 2 mm/year vertical rate of deformation during the last 100 years (Berg, 1994; Mälzer et al., 1983) combined with the seismic activity are the most significant elements for recent and present-day crustal deformation. Based on the main geological structures and Cenozoic subsidence data, the LRE can be divided into several tectonic units (Fig. 7): the Krefeld Block to the northeast, the Venlo and Peel Blocks to the north, the Roer Graben and the Erft Block in the centre, the Campine, the South Limburg Blocks and the Brabant Block, bordering the subsiding area to the southwest (Camelbeek, 2000). The Roer Graben is

Fig. 5. Intensity and direction gradient images for models with a conductive top layer. The dotted lines represent the synthetic model. The electrical tomography of the model is shown above each gradient image. The resistivity scale is the same for all tomographies. Gradient intensity image (bottom) of a vertical contact with a 1 m (A), 4 m (B) and 6 m (C) 20 Ω m top layer. (D) Dipping model intensity (middle) and direction (bottom) gradient images with a 2 m 20 Ω m top layer. (E and F) Gradient intensity image (bottom) of a step-like model with a 1.5-m step height and respectively a 10 Ω m and 20 Ω m top layer (2 m thick). (G and H) Gradient intensity image (bottom) of a step-like model with a 1.5-m step height and respectively a 10 Ω m and 20 Ω m top layer (1 m thick). (I) Gradient intensity image (bottom) of a step-like model with a 3-m step height and a 2 m and 20 Ω m top layer.

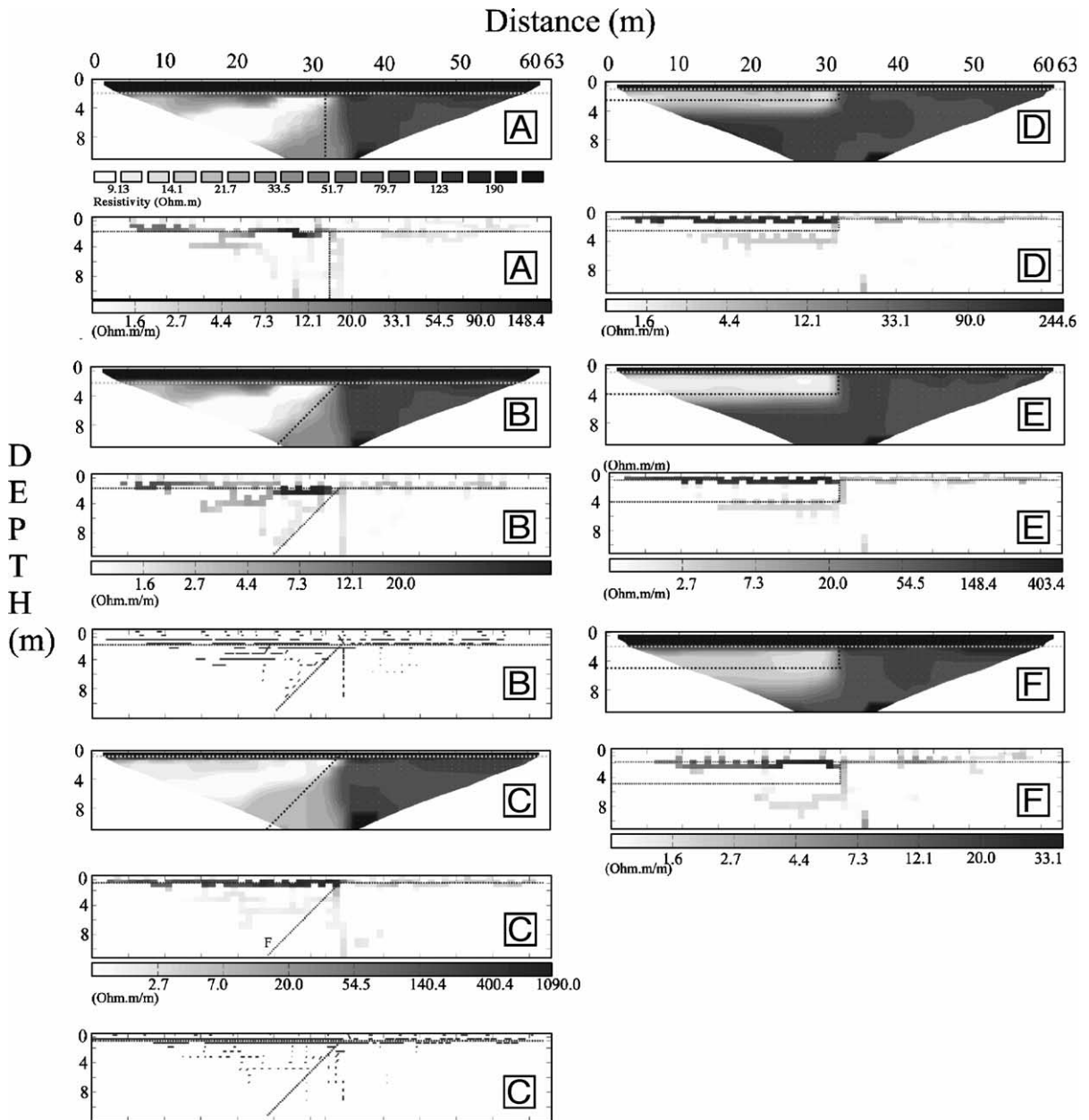


Fig. 6. Intensity and direction gradient images for models with a resistive ($250 \Omega \text{ m}$) top layer. The dotted lines represent the synthetic model. The electrical tomography of the model is shown above each gradient image. The resistivity scale is the same for all tomographies. (A) Gradient intensity image (bottom) for a vertical model with top layer of 2 m. (B) Intensity (middle) and direction (bottom) gradient images for a dipping model with a top layer of 2 m. (C) Intensity (middle) and direction (bottom) images for a dipping model with a top layer of 1 m. (D and E) Intensity gradient images (bottom) for a step-like model with a top layer of 1 m and with respectively a step height of 1.5 m and 3 m. (F) Intensity gradient images (bottom) for a step-like model with a 2 m top layer and a step height of 3 m.

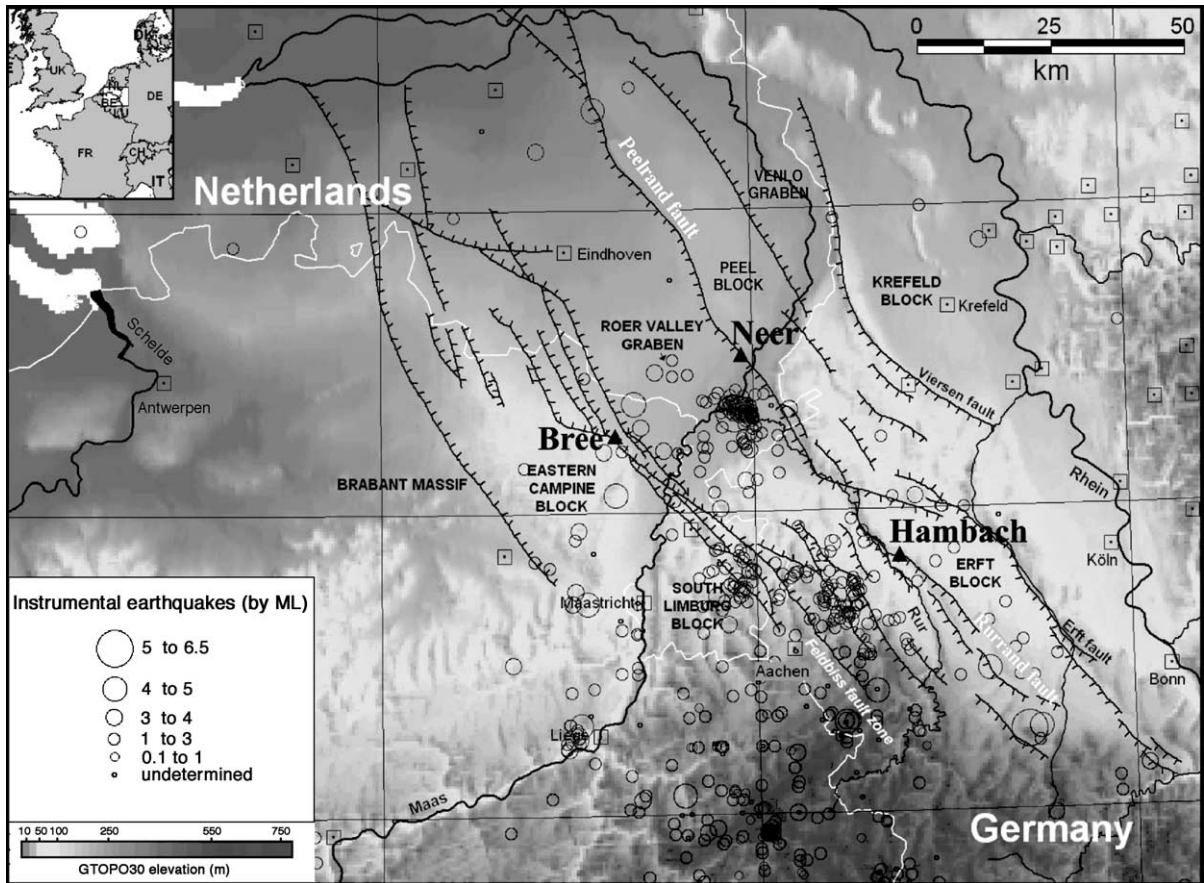


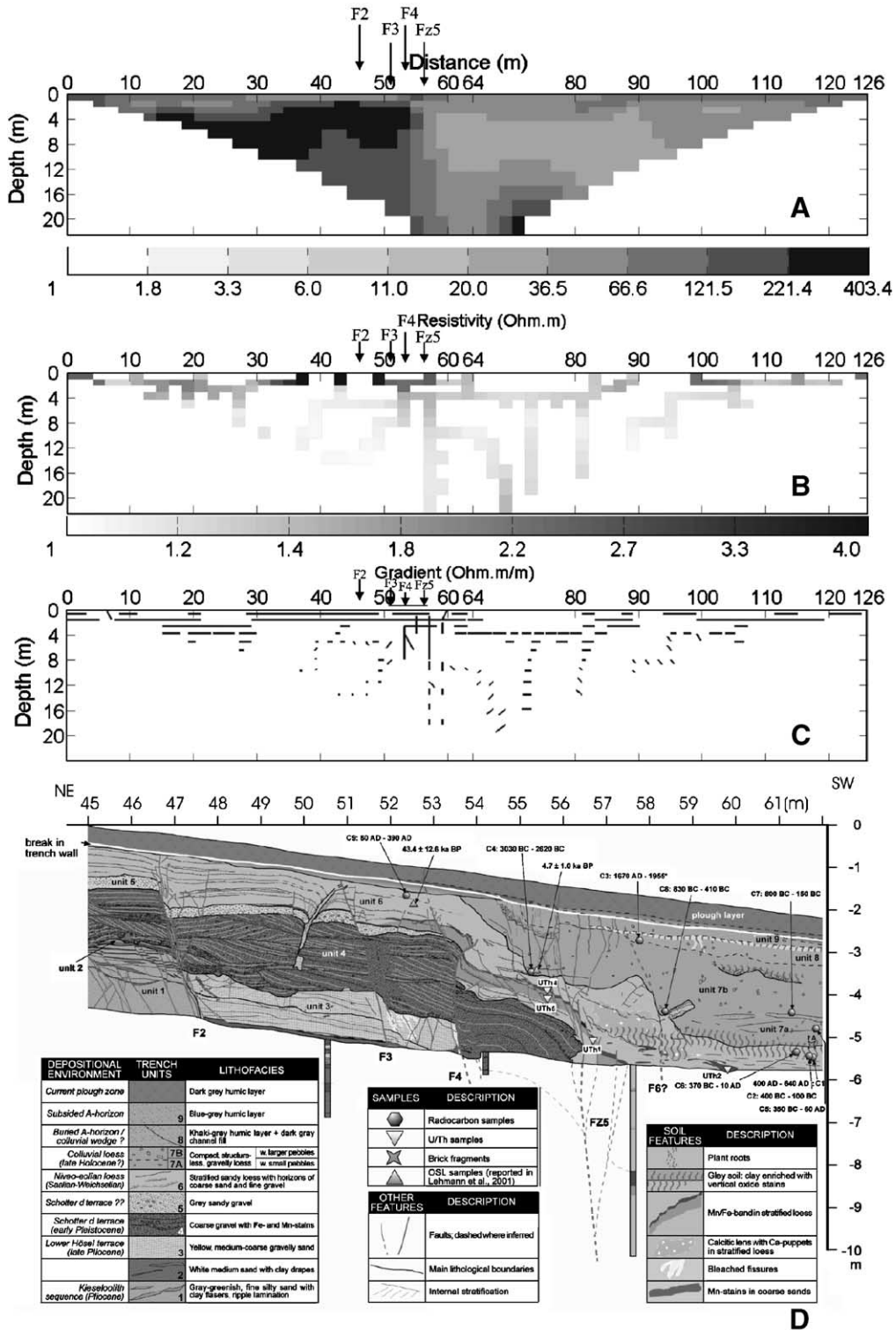
Fig. 7. Location of the PALEOSIS sites: seismotectonic map of the Lower Rhine System, red triangles show the location of the three areas (Bree, Neer and Hambach) where paleoseismic investigations were conducted during the PALEOSIS project (modified from Vanneste et al., 2001).

bordered by two main NNW–SSE trending Quaternary normal fault systems, the Peelrand Fault (see *site of Neer*), which continues as the Rurrand fault in Germany (see *site of Hambach*) to the east and the Feldbiss Fault (see *site of Bree*) to the west (Camelbeek, 2000).

During the PALEOSIS project, location of trenches has been derived successfully from different geophysical measurements, including electrical tomography. Data sets on three sites have been chosen to illustrate the application of the gradient method tested on synthetic cases.

The first site, Hambach, is situated in Germany along the Rurrand fault (Fig. 7). The trench, shown in Fig. 8D, exposes silt and loess in the hanging wall, while the footwall is made of coarse sands, gravel and sandy loess near the surface (Vanneste and Verbeek,

2001). Trench studies (Fig. 8D) reveal a complex fault zone consisting of several SW-dipping normal fault strands characterized by different histories of activity. Overall, four splayed branches (labelled F2, F3, F4 and FZ5 on Fig. 8) reach almost 1 m below the surface. All faults displace a 2-m-thick, iron-stained, coarse gravel unit, as well as an overlying sandy loam unit (Vanneste and Verbeek, 2001). Since deposition of the gravel unit, the cumulative vertical displacement reaches at least 70 cm. The faults occur at 46.5 (F2), 51 (F3), 53 (F4) and 56 m (FZ5) with a vertical displacement respectively of 65, 30, 105 and over 500 cm (Vanneste and Verbeek, 2001). Coseismic slip seems to be the dominant mode of fault movement, whereas no evidence for growth faulting has been found (Vanneste and Verbeek, 2001). Fig. 8 presents an electrical tomography performed on the site (Jongmans, 2000).



D

The electrical contrast between the juxtaposed blocks is 250–400 Ω m to 30–60 Ω m and the superficial plough layer is very thin (<1 m). The lateral contrast results from a lateral variation in soil nature. Fig. 8B and C show the gradient images (respectively the intensity and the direction images) computed from the tomography. It appears that the main gradients near the surface are horizontal contacts and that two vertical limits are clearly found at 53 and 56 m. These two limits probably correspond to the major fault zone with the largest vertical displacement (respectively F4 and FZ5), although the exact location is highly dependent of the resolution (pixel size). Clearly, the MDG images provide an accurate location of the main fault zone, whereas the visual interpretation would lead to one broader limit, located between 52 and 60 m, depending on the colour scale and on the interpreter.

The second site (Bree IV) is located near Bree in the Lower Rhine Embayment (Fig. 9). The trench studies (Fig. 9D) reveal a fault located at 56 m (F on Fig. 9) along the profile (Vanneste et al., 2001). Trenching exposed coarse, clayey and gravely Maas River sediments corresponding to the Zutendaal gravels in the footwall, juxtaposed by a narrow fault zone to more fine-grained, partly reworked cover sands with some gravel horizons in the down thrown block. Two wedges of reworked Maas material are present in the hanging wall close to the fault, wedging out downslope, whereas the main Maas River terrace is probably down thrown beneath the trench bottom (Vanneste et al., 2001). Fig. 9A shows the electrical tomography (Demagnet et al., 2001b) while Fig. 9B and C present the gradient intensity and direction images, respectively. The electrical tomography is mainly characterized by a relatively uniform resistivity ranging between 180 and 240 Ω m, with a lateral gradient around 60 m. This disturbance probably corresponds to a depth variation in the water table, which was at least at 6 m in the footwall and at more than 9 m in the hanging wall, as indicated by hand borings (Demagnet et al., 2001b; Vanneste et al., 2001). The weak lateral electrical contrast, 180 to 240 Ω m, and the very resistive superficial layer (>500 Ω m) make the application of the MDG methodology

difficult, as predicted by the synthetic study. Indeed, it is unclear where to locate a fault on the intensity gradient image. A zone ranging from 50 to 64 m and near 80 m shows vertical limits at medium and greater depth (Fig. 9B). The direction image exhibits two shallow and tenuous vertical contacts slightly before 56 m, where a fault is observed in the trench (Fig. 9C) as well as weaker limits located at depth at the same horizontal distance (corresponding to the ones observed in the gradient intensity image). Although the MDG method provides less clear indications of a vertical contact than for Hambach, it gives a fault zone near the one observed in the trench.

Our last example is presented on Fig. 7 which shows the electrical tomography (A) performed at Neer along the Peel fault (Jongmans, 2000), in the Lower Rhine Embayment (Fig. 7). A fault (F) is located in the trench at 55.5 m (Fig. 10D, Berg et al., 2002). The sedimentology of the exposed sediments shows a transition from a fluvial aggradation-terrace (SW), into an Aeolian sand sheet (NE). The overlying sand sheet is about 1.5 m thick. From the electrical tomography, we can see that the lateral electrical contrast is very low (40 to 90 Ω m at depth and 400 to 300–350 Ω m near the surface) and the superficial layer is highly resistive, as observed on the site of Bree IV. The low-resistivity values are probably due to the presence of a shallow water level table. On this site, no indication of a vertical contact can be derived from the gradient intensity or direction images (Fig. 10B and C). Unlike the Bree IV site, with similar conditions, the MDG interpretation does not give any clue of where to locate a fault, nor does the visual interpretation. This unveils a major limitation of the method, linked to the basic tool (MDG) that was used throughout this study and the real field conditions. As a maximum of directional gradient is computed to separate the different geological units, one has to assume that the horizontal gradient is the largest at the contact when looking at near-vertical limits. However, this methodology does not work if the vertical gradient (horizontal limit) is larger than the horizontal one, which is likely to occur in real geological conditions. Therefore, if the layer is too thin or the horizontal gradient too low, the MDG algorithm

Fig. 8. Electrical tomography (A), intensity (B) and direction (C) gradient images performed on the site of Hambach. F2, F3, F4 and FZ5 mark observed fault branches in trench. (D) Trench log (Vanneste and Verbeeck, 2001).

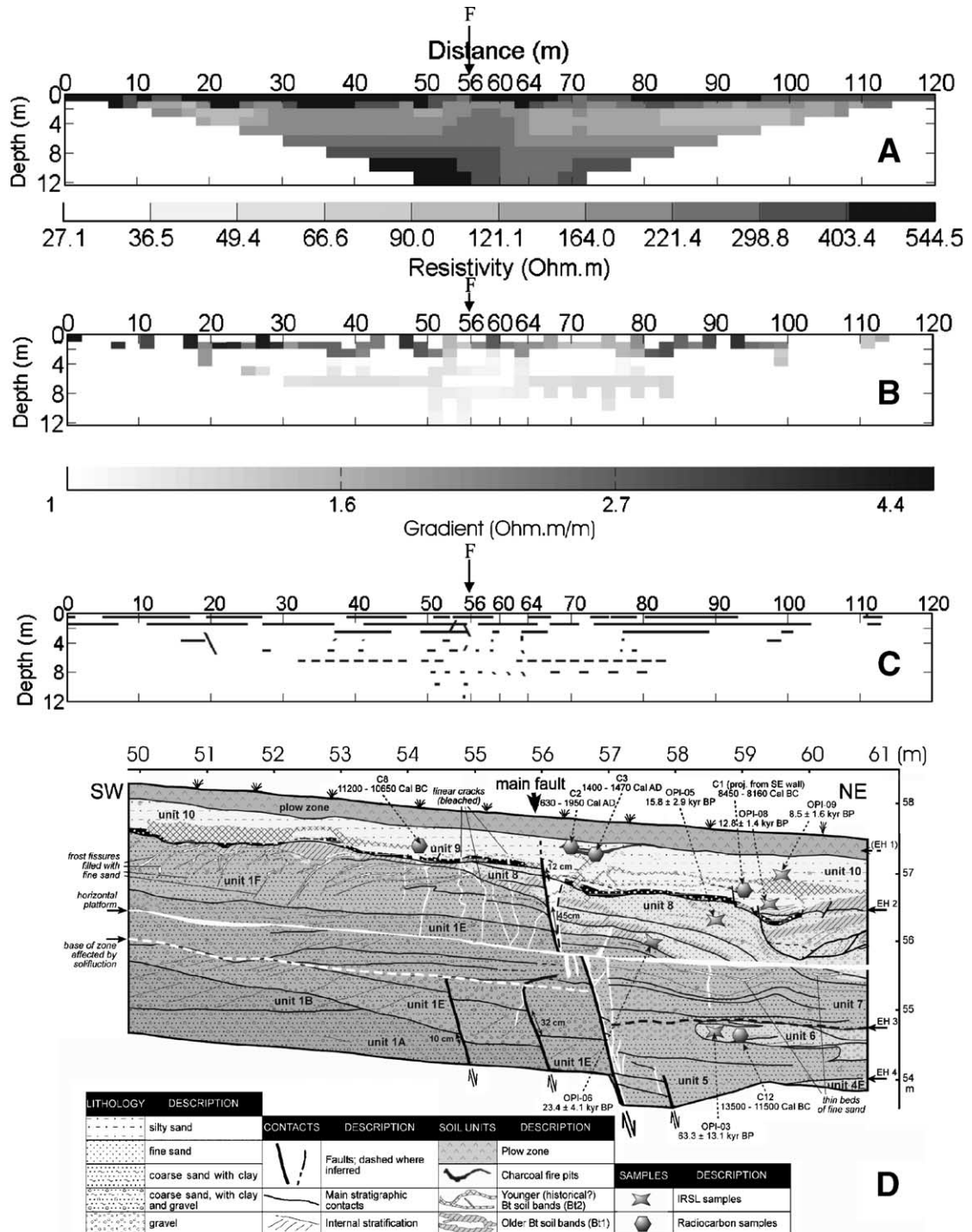


Fig. 9. Electrical tomography (A), intensity (B) and direction (C) gradient images performed on the site of Bree IV. F marks the location of the observed fault in trench. (D) Trench log (Vanneste et al., 2001).

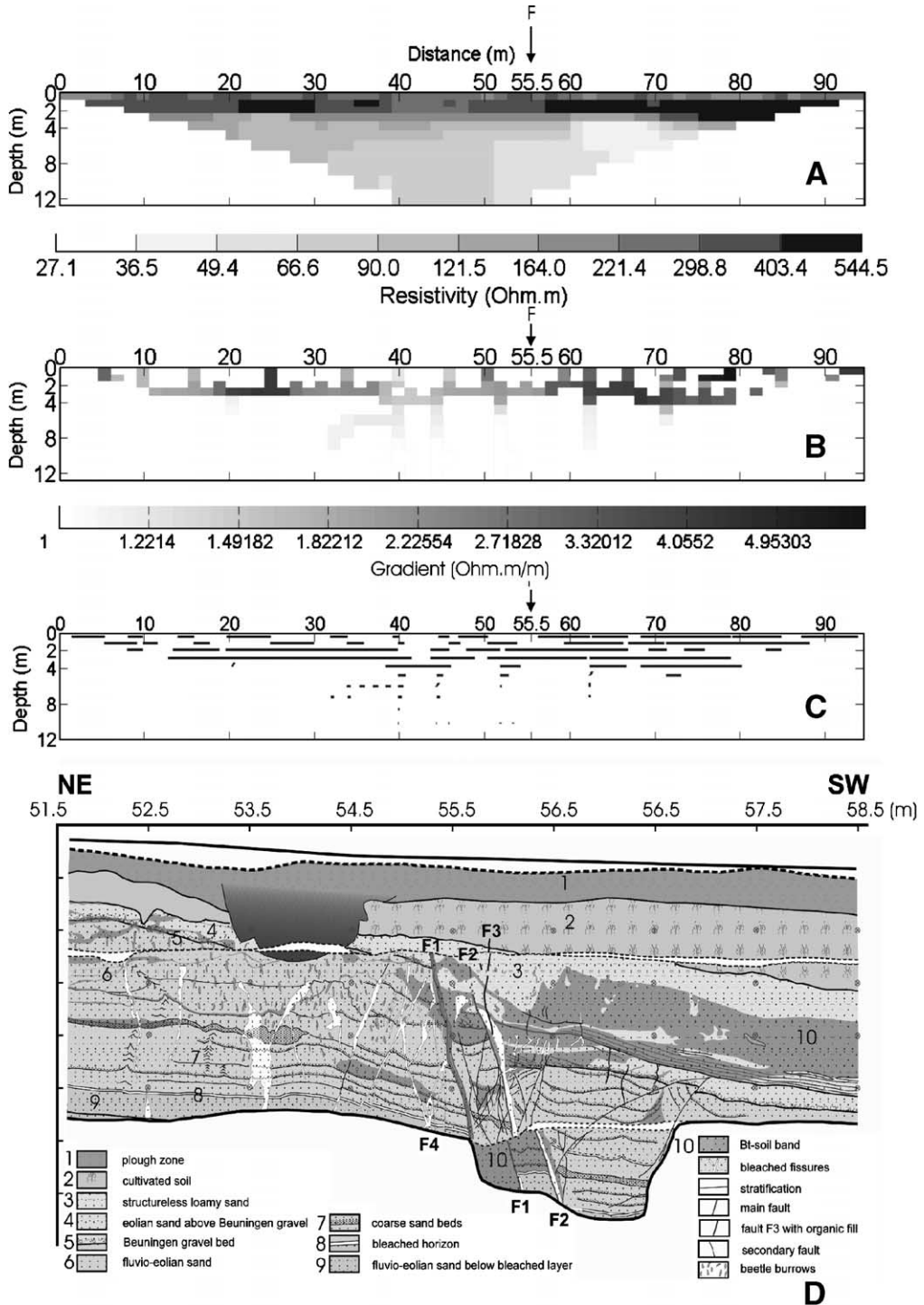


Fig. 10. Electrical tomography (A), intensity (B) and direction (C) gradient images performed on the site of Neer. F marks the location of the observed fault in trench. (D) Trench log (Berg et al., 2002).

automatically points out the horizontal limit and disregards the vertical one which is the targeted limit. Thus, other algorithms should be tested in the future to furthermore explore their potential in quantifying the information on tomographies. For example, the use of a directional gradient, which needs further developments, could overcome these effects.

5. Conclusion

A maximum of directional gradient (MDG) algorithm is applied on electrical images with the aim of automatically locating near vertical boundaries between geological units (in this case, faults) and of determining layer displacement. Tests made on synthetic data (a simple fault model and a step-like model, with a top layer) show that the method is efficient in most cases. Very satisfying results are obtained for sites presenting a high lateral electrical contrast and a thin (up to 4 m for a conductive top layer and 2 m for a resistive one) superficial layer. When the lateral electrical contrast is smaller (ratio less than 0.75 according to the field data) and the layer is thicker and/or more resistive, the resolution decreases and results are more ambiguous but some indications of a vertical contact can still be deduced. For very low lateral contrasts and with the presence of a resistive top layer, no fault evidence is found on gradient images. On the contrary, the horizontal limits (bedding) are well retrieved for both models. The results on synthetic data have been corroborated by field data processing. A further improvement of the method could be the use of directional gradients. One major advantage of the method, shown on synthetic data, is the objectiveness of the processing, comparing to a visual interpretation which is usually biased by the scale and colour choices. Such gradient methods could also be used for any survey whose target is to locate a sharp boundary (such as bedrock depth estimation, contamination plumes and karst geometry).

Acknowledgments

We thank Thierry Camelbeeck, Kris Vanneste, Koen Verbeek from the Royal Observatory of Belgium for providing us the E.U. PALEOSIS project

(ENV4-CT97-0578) data, and in particular, Kris Vanneste for providing us figures of the trenches and maps. This research was carried out within the scope of the E.U. SAFE project (EVG1-2000-22005). We thank our reviewers, Prof. Dr. Koichi Suzuki and an anonymous reviewer, for their thorough reviews and constructive comments on the manuscript. LIRIGM is a member of the French RNVO (Risques Naturels et Vulnérabilité des Ouvrages) network.

References

- Al-Nuaimy, W., Huang, Y., Nakhkash, M., Fang, M.T.C., Nguyen, V.T., Eriksen, A., 2000. Automatic detection of buried utilities and solid objects with GPR using neural networks and pattern recognition. *Journal of Applied Geophysics*, 43, 157–165.
- Barker, R.D., 1989. Depth of investigation of collinear symmetrical four-electrode arrays. *Geophysics*, 54, 1031–1037.
- Berg, M.W. van den, 1994. Patterns and velocities of recent crustal movements in the Dutch part of the Roer Valley rift system. *Geologie & Mijnbouw*, 73, 157.
- Berg, M.W. van den, Vanneste, K., Dost, B., Lokhorst, A., Eijk, M. van, Verbeek, K., 2002. Paleoseismic investigations along the Peel Boundary Fault: geological setting, site selection and trenching results. *Netherlands Journal of Geosciences/Geologie & Mijnbouw*, 81 (1), 39–60.
- Bergeron, S.Y., Yuen, D.A., 2000. Capabilities of 3-D wavelet transforms to detect plume-like structures from seismic tomography. *Geophysical Research Letters*, 27 (20), 3433–3436.
- Beucher, S., Meyer, F., 1992. The morphological approach to segmentation: the watershed transformation. In: Dougherty, E. (Ed.), *Mathematical Morphology in Image Processing*. Marcel Dekker, New York, pp. 433–481.
- Camelbeeck, T., 2000. PALEOSIS (ENV4-CT97-0578) Final report: evaluation of the potential for large earthquakes in regions of present day low seismic activity in Europe.
- Camelbeeck, T., Meghraoui, M., 1996. Large earthquakes in northern Europe more likely than once thought, EOS, *Transactions*. AGU, 77 (42), 405–409.
- Camelbeeck, T., Meghraoui, M., 1998. Geological and geophysical evidence for large paleoearthquakes with surface faulting in the Roer Graben (northwest Europe). *Geophysical Journal International*, 132, 347–362.
- Carter, N., Lines, L., 2001. Fault imaging using edge detection and coherency measures on Hibernia 3-D seismic data. *The Leading Edge*, 20 (01), 64–69.
- Claerbout, J.F., Muir, F., 1973. Robust modeling with erratic data. *Geophysics*, 38, 826–844.
- Dahlin, T., Bernstone, C., Loke, M.H., 2002. A 3-D resistivity investigation of a contaminated site at Lernacken, Sweden. *Geophysics*, 67 (6), 1692–1700.
- deGroot-Hedlin, C., Constable, S., 1990. Occam's inversion to generate smooth, two dimensional models from magnetotelluric data. *Geophysics*, 55, 1613–1624.

- Demagnet, D., Pirard, E., Renardy, F., Jongmans, D., 2001a. Application and processing of geophysical images for mapping faults. *Computers & Geosciences*, 27, 1031–1037.
- Demagnet, D., Renardy, F., Vanneste, K., Jongmans, D., Camelbeeck, T., Meghraoui, M., 2001b. The use of geophysical prospecting for imaging active faults In the Roer Graben, Belgium. *Geophysics*, 66 (1), 78–89.
- Geluk, M.C., Duin, E.J.T., Dusar, M., Rijkers, R.H.B., van den Berg, M.W., van Rooijen, P., 1994. Stratigraphy and tectonics of the Roer Valley Graben. *Geologie & Mijnbouw*, 73, 129.
- Jongmans, D., 2000. Final technical report on the activity Université de Liège—LGIH Development and application of geophysical prospecting for fault detection and characterization purposes, PALEOSIS (ENV4-CT97-0578) Final Report: Evaluation of the potential for large earthquakes in regions of present day low seismic activity in Europe.
- Loke, M.H., Barker, R.D., 1996. Rapid least-squares inversion of apparent resistivity pseudosections by a quasi-Newton method. *Geophysical Prospecting*, 44, 131–152.
- Loke, M.H., Dalhin, T., 2002. A comparison of the Gauss–Newton and quasi-Newton methods in resistivity imaging inversion. *Journal of Applied Geophysics*, 49, 149–462.
- Loke, M.H., Acworth, I., Dalhin, T., 2003. A comparison of smooth and blocky inversion methods in 2-D electrical imaging surveys. *Exploration Geophysics*, 34, 182–187.
- Louis, I.F., Raftopoulos, D., Goulis, I., Louis, F.I., 2002. Geophysical Imaging of faults and fault zones in the urban complex of Ano Liosia Neogene basin, Greece: synthetic simulation approach and field investigations. *International Conference on Earth Sciences and Electronics*.
- Mälzer, H., Hein, G., Zippelt, K., 1983. Height changes in the Rhenish massif: determination and analysis. In: Fuchs, K., et al., (Eds.), *Plateau Uplift*. Springer Verlag.
- Meads, N.L., Bentley, L.R., Mendoza, C.A., 2003. Application of electrical resistivity imaging to the development of a geologic model for a proposed Edmonton landfill site. *Canadian Geotechnical Journal*, 40, 551–558.
- Morozov, L.B., Smithson, S.B., 1996. High-resolution velocity determination: statistical phase correlation and image processing. *Geophysics*, 61 (4), 1115–1127.
- Nguyen, F., Garambois, S., Chardon, D., Jongmans, D., Bellier, O., Hermitte, D., 2003. Slow active fault detection and imaging using multiple geophysical methods: the Trévaresse thrust (Provence, France). *Geophysical Research Abstracts*, 5, 10878.
- Olayinka, A.I., Yaramanci, U., 2000. Assessment of the reliability of 2D inversion of apparent resistivity data. *Geophysical Prospecting*, 48, 293–316.
- Oldenburg, D.W., Li, Y., 1999. Estimating depth of investigation in dc resistivity and IP surveys. *Geophysics*, 64, 403–416.
- Pessel, M., 2000. Tomographie de résistivité électrique : Développements méthodologiques et applications. Thèse de 3ème cycle de l'Université de Rennes I, Mémoires de Géosciences Rennes, 98, 129 pp.
- Press, W.H., Flannery, B.P., Teukolsky, S.A., Vetterling, W.T., 1988. *Numerical Recipes in C*. Cambridge Univ. Press, Cambridge, UK.
- Sambridge, M., 1999a. Geophysical inversion with a neighbourhood algorithm: I. Searching a parameter space. *Geophysical Journal International*, 138, 479–494.
- Sambridge, M., 1999b. Geophysical inversion with a neighbourhood algorithm: II. Appraising the ensemble. *Geophysical Journal International*, 138, 727–746.
- Sasaki, Y., 1992. Resolution of resistivity tomography inferred from numerical simulation. *Geophysical Prospecting*, 40, 453–464.
- Suzuki, K., Toda, S., Kusunoki, K., Fujimitsu, Y., Mogi, T., Jomori, A., 2000. Case studies of electrical and electromagnetic methods applied to mapping active faults beneath the thick quaternary. *Engineering Geology*, 56, 29–45.
- Tarantola, A., 1987. *Inverse Problem Theory*. Elsevier, Amsterdam.
- Vanneste, K., Verbeeck, K., 2001. Paleoseismological analysis of the Rurand fault near Jülich, Roer Valley graben: Coseismic or aseismic faulting history? *Netherlands Journal of Geosciences*, 80 (3–4), 155–169.
- Vanneste, K., Verbeeck, K., Camelbeeck, T., Paulissen, E., Meghraoui, M., Renardy, F., Jongmans, D., Frechen, M., 2001. Surface-rupturing history of the Bree fault scarp, Roer Valley graben: evidence for six events since the late Pleistocene. *Journal of Seismology*, 5, 329–359.
- van Schoor, M., 2002. Detection of sinkholes using 2D electrical resistivity imaging. *Journal of Applied Geophysics*, 50, 393–399.
- Vasudevan, K., Tozser, P., Cook, F.A., 1997. Delineation of surfaces by skeletonization: application to interpretation of 3D seismic reflection and georadar data volumes. *Geophysical Research Letters*, 24 (7), 767–770.
- Vincent, L., Soille, P., 1991. Watersheds in digital spaces: an efficient algorithm based on immersion simulations. *IEEE Transactions on Pattern Analysis and Machine Intelligence*, 13 (6), 583–598.
- Wise, D.J., Cassidy, J., Locke, C.A., 2003. Geophysical imaging of the Quaternary Wairoa North Fault, New Zealand: a case study. *Journal of Applied Geophysics*, 53, 1–16.